analytical chemistry

pubs.acs.org/ac Article

Development of Hollow Electrochemiluminescent Nanocubes Combined with a Multisite-Anchored DNA Nanomachine for Mycotoxin Detection

Xia Zhong,[§] Shan-Shan Yang,[§] Ni Liao, Ruo Yuan, and Ying Zhuo*

Cite This: *Anal. Chem.* 2021, 93, 5301−5308 Read Online

ACCESS | Metrics & More | Article Recommendations | Supporting Information

ABSTRACT: Polycyclic aromatic hydrocarbons (PAHs) are regarded as promising electrochemiluminescent (ECL) emitters owing to their high quantum efficiency and inexpensive production. Despite the fact that the ECL properties of the pure PAH microcrystal (such as rubrene microcrystals, Rub MCs) have gained extensive attention, it is a challenge in controlling the morphology and size to reduce the inner filter effect. Herein, an advanced ECL emitter of palladium nanoparticle-functionalized hollow PAH-metal nanocubes was prepared by an in situ redox deposition method (the resultant nanocomposites were abbreviated as Pd-Rub-Ag@Au nanocubes). Specifically, the rubrene-decorated Ag@Au nanocubes (Rub-Ag@Au nanocubes) were prepared using the Ag@Au nanocubes as a template and a rubrene cation radical ($Rub^{\bullet+}$) as a reductant, and then Pd nanoparticles (Pd NPs) were in situ reduced on the surface of Rub-Ag@Au nanocubes. Impressively, compared with the Rub MCs, Pd-Rub-Ag@Au nanocubes showed uniform size and significantly enhanced ECL efficiency and intensity in the aqueous media. As a proof-of-concept, the Pd-Rub-Ag@Au nanocube-based ECL biosensing platform combined with a multisite-anchored DNA nanomachine was constructed for ochratoxin A (OTA, a type of mycotoxin) detection. The DNA nanomachine covered with high-density recognizing sequences could operate toehold-mediated strand displacement amplification on the sensing platform and promote the movement efficiency and velocity greatly. Due to the advanced performance of Pd-Rub-Ag@Au nanocubes and high recognition efficiency of the DNA nanomachine, the proposed biosensor for OTA detection can achieve a detection limit of 4.7 fg/mL ranging from 0.01 to 100 pg/mL, which offers an ingenious method for the further application of PAHs.

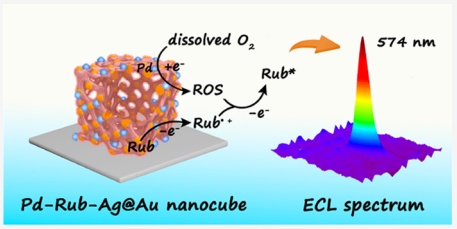

1. INTRODUCTION

During the past decades, numerous polycyclic aromatic hydrocarbons (PAHs), such as tetraphenylethylene (TPE), phenanthrene derivatives, perylene derivatives, rubrene (Rub), and 9,10-diphenylanthracene (DPA), had been widely used in biosensing, bioimaging, advanced organic devices, and so on, owing to their high quantum efficiency and inexpensive production.[1−7] However, these PAHs with aromatic structures were hardly applied in the field of electrochemiluminescent (ECL) bioanalysis due to the low radical ion stability and weak solubility, which caused weak and unstable ECL response in aqueous media. Recently, the surfactant-assisted self-assembly method was applied to synthesize the ECL PAHs nano-/microcrystals for the ECL intensity and stability improvement in the aqueous media, which realized the potential application in bioanalysis. Our previous work demonstrated that the ECL intensity of TPE nanocrystals (TPE NCs) in the aqueous media was 20-fold higher than that of the free TPE molecules.[8] Although the ECL intensity and stability of the PAHs nano-/microcrystals have been improved apparently, the spectra depending on their morphology and uniformity were easily affected by the preparation conditions, such as the amount and types of surfactants, reaction time, and heat treatment. Meanwhile, the dense stacking of the plane conjugated molecules in these bulk nano-/microcrystals also caused the inner filter effect, which restricted the luminous intensity and efficiency. Thus, the development of PAH nanomaterials with a uniform size and high ECL efficiency was regarded as a meaningful and challenging task. In this work, the palladium nanoparticle-functionalized hollow PAH-metal nanocubes (Pd-Rub-Ag@Au nanocubes) were first synthesized with Ag@Au nanocubes as a template and $Rub^{\bullet+}$ as a reductant through an in situ redox deposition method, then in situ generating Pd nanoparticles (Pd NPs) on the surface (Scheme 1A). Thanks to the uniform hollow structure, Pd-Rub-Ag@Au nanocubes possessed a desirable ECL efficiency with the rubrene molecules as emitters, dissolved O_2 as a coreactant, and Pd NPs as a coreaction accelerator, which achieved a high-intense ECL response in the aqueous media.

In situ nucleic acid amplification methods are valuable tools for trace target detection in a complex background. With the

Received: January 30, 2021
Accepted: March 9, 2021
Published: March 19, 2021

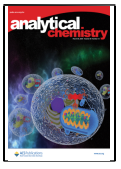

https://doi.org/10.1021/acs.analchem.1c00446
Anal. Chem. 2021, 93, 5301−5308

Scheme 1. Schematic Illustration of the (A) Preparation Process of the Hollow Pd-Rub-Ag@Au Nanocubes, (B) OTA-Induced Hairpin Assembly Enzyme-Powered Cyclic Amplification Process-Based Multisite-Anchored DNA Nanomachines, and the (C) Detection Process of the Biosensor

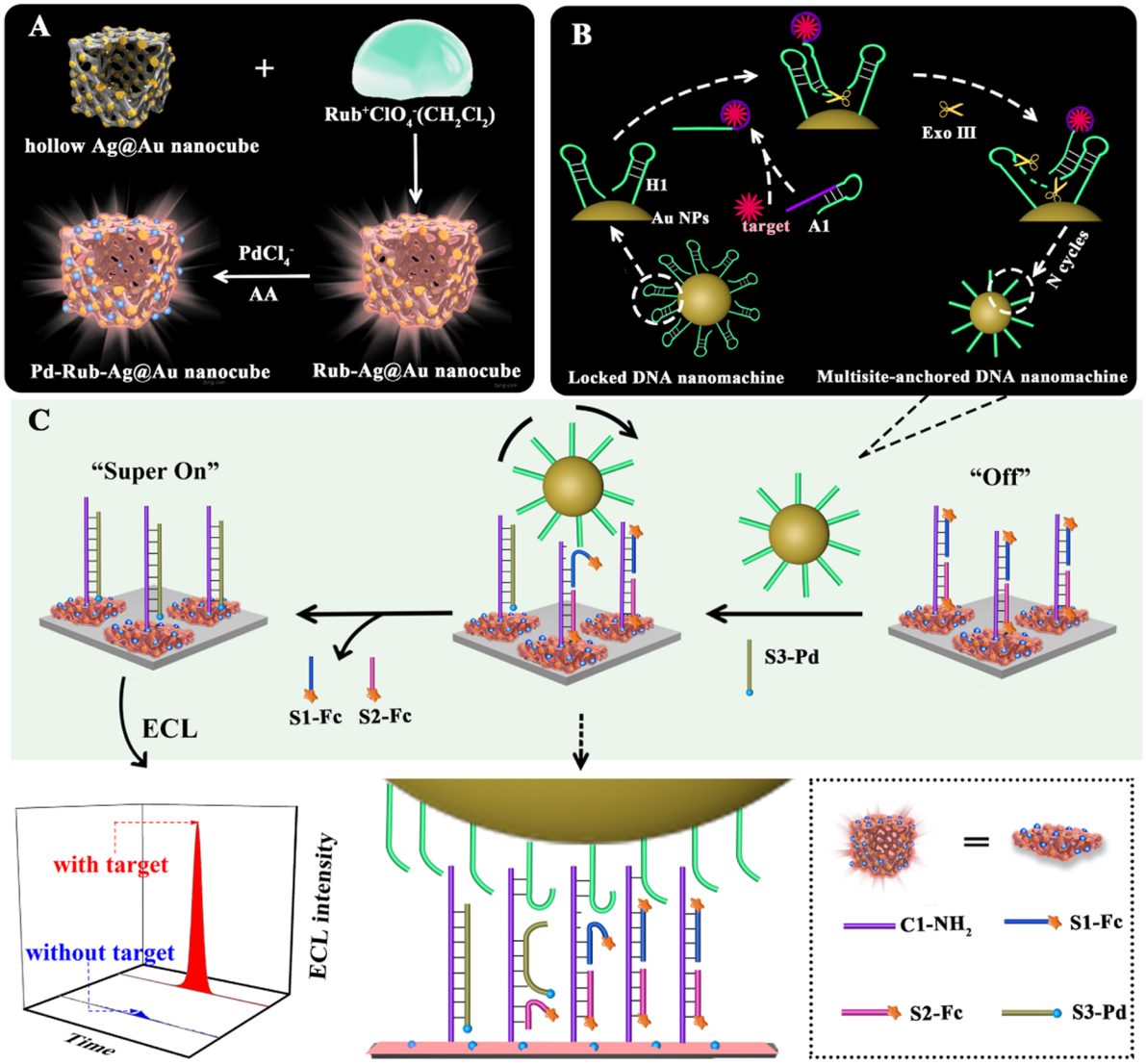

help of various target transformation strategies based on nucleic acid amplification techniques, such as the hybridization chain reaction (HCR)[9] and strand displacement amplification (SDA),[10] the detection sensitivity and specificity have been greatly improved, especially for the non-nucleic acid target.[11,12] Lately, 3D DNA nanomachines have provided a desirable avenue for the recognition efficiency promotion due to their nonequilibrium systems driven by dynamic interactions. For example, Li's group designed an enzyme-powered DNA nanomachine to rapidly cleave payloads during the movement, resulting in rapid, isothermal, and homogeneous signal amplification.[13] In our previous work, a 3D DNA machine assembled by DNA nippers could hybridize with target microRNA to recover the ECL signal of $Ru(bpy)_2^{2+}$, improving the recognition efficiency significantly.[14] However, these 3D DNA machines were executed in a homogeneous solution to release single-strand DNAs dispersed in the reaction solution randomly, which were difficult to be captured on the sensing platform and inclined to spontaneous off-track during movement, causing the low velocity and moving efficiency. Thus, it is of critical significance to integrate more specific recognition sites and higher moving efficiency within one alternative DNA nanomachine.

Thereupon, to address the above issues, a multisite-anchored DNA nanomachine was designed to execute a heterogeneous interface for the sensitive detection of ochratoxin A (OTA, a foodborne mycotoxin with the potential carcinogenicity, nephrotoxic, and immunosuppression) with the Pd-Rub-Ag@Au nanocube-based biosensing platform.[15] Briefly, the locked DNA nanomachine was obtained by the assembly of hairpin probes H1 on gold nanoparticles (Au NPs). With the target and its corresponding aptamer, the hairpin probes were cleaved with the aid of exonuclease III (Exo III) to execute the target conversion process based on the cycle recognitions of a target−aptamer complex, which gradually activated the multisite-anchored DNA nanomachine, as shown in Scheme 1B. Notably, the activated DNA nanomachine processed a high local concentration of the recognition sequence on its surface, which could provide multisites to operate toehold-mediated strand displacement amplification on the sensing platform and

https://doi.org/10.1021/acs.analchem.1c00446
Anal. Chem. 2021, 93, 5301−5308

promote the movement efficiency and velocity greatly. On the other hand, Pd-Rub-Ag@Au nanocubes were prepared and assembled on the glass carbon electrode (GCE) to obtain a strong initial signal with dissolved O_2 as the endogenous coreactant (Scheme 1A). Subsequently, the quenching probes (S1-Fc and S2-Fc, both labeled by ferrocene molecules) were bonded to the hollow Pd-Rub-Ag@Au nanocubes by a Pd−N bond for reducing the initial signal, which presented a "signal off" state, as shown in Scheme 1C. When the target OTA induced the DNA nanomachine to be activated, the movement and loading of enhancer probes (S3 DNA labeled by Pd NPs, S3-Pd) drove the quenching probes to leave the electrode surface, which achieved a "signal super on" state (Scheme 1C). This work not only provided a promising method to obtain the advanced PAH-based ECL luminophore with the in situ redox deposition route but also applied the multisite-anchored DNA nanomachines in the ECL analysis to achieve the efficient and rapid detection of the target.

2. EXPERIMENTAL METHODS

2.1. Synthesis of Hollow Pd-Rub-Ag@Au Nanocubes. Hollow Pd-Rub-Ag@Au nanocubes as new ECL luminophores were prepared by the redox reaction between hollow Ag@Au nanocubes and rubrene perchlorate ($Rub^+ClO_4^-$), whose preparation approaches are present in detail as follows.

2.1.1. Preparation of a $Rub^+ClO_4^-$ Solution.[16] First, 10 mg of Rub was dissolved into 3 mL of anhydrous dichloromethane (CH_2Cl_2) with moderate stirring. Meanwhile, 3.9 mg of silver perchlorate ($AgClO_4$) was dispersed in 200 μL of anhydrous acetonitrile (CH_3CN). Then, the $AgClO_4$ solution was injected into the Rub solution under stirring. After the iodine (I_2) solution (2.4 mg I_2 in 240 μL CH_2Cl_2) was added into the obtained mixture, the color of the resultant solution changed immediately from orange to olive-drab, producing a large amount of white precipitates. When the reaction lasted for 20 min, the olive-drab solution ($Rub^+ClO_4^-$ solution) was collected by centrifugation. Subsequently, the solution was dried overnight under vacuum at room temperature. Finally, the obtained solid was dissolved in 2 mL of CH_3CN and stored in the dark.

2.1.2. Preparation of Hollow Ag@Au Nanocubes.[17] To prepare the hollow Ag@Au nanocubes, 90 μL of a 1% gold chloride tetrahydrate ($HAuCl_4$) solution was added into 20 mL of ultrapure water to obtain a uniform solution. Next, 340 μL of 6 mM silver nitrate ($AgNO_3$) was added into the $HAuCl_4$ solution under stirring to obtain a milky white muddy solution. Then, 1 mL of 100 mM L-ascorbic acid (AA) was injected into the resultant solution. Immediately, the solution turned in the evident blue color, which indicated the generation of the hollow Ag@Au nanocubes. Subsequently, the obtained mixture was kept still for 10 min. Finally, the as-prepared products (Ag@Au nanocubes) were collected by centrifugation (2500 rpm, 20 min) and resuspended in 5 mL of a CH_3CN solution.

2.1.3. Preparation of Hollow Pd-Rub-Ag@Au Nanocubes.[18] First, 8 mL of a solution containing the as-synthesized Ag@Au nanocubes in CH_3CN was added dropwise into 1 mL of the above $Rub^+ClO_4^-$ solution under vigorous stirring. After 30 min, the color of the mixture was darkened, illustrating the formation of the Rub-Ag@Au nanocubes. Next, 20 μL of a 5 mM potassium tetrachloropalladate(II) (K_2PdCl_4) solution was injected into the Rub-Ag@Au nanocubes solution to stir for 40 min. Then, 200 μL of a 100 mM AA solution was slowly added into the above mixture drop by drop to react for another 2 h. Subsequently, the hollow Pd-Rub-Ag@Au nanocubes were collected by centrifugation and washed three times using deionized water. Eventually, the obtained hollow Pd-Rub-Ag@Au nanocubes were resuspended in 5 mL of deionized water for further use.

2.2. Preparation of Locked DNA Nanomachines. First, 400 μL of a solution of 2.5 μM H1 (5′-SH modified DNA strand) was annealed to obtain the hairpin structure and then reduced by 20 μL of 10 mM tris-(2-carboxethyl)-phosphine hydrochloride (TCEP) for 1 h to obtain sulfydryl groups.[19] Subsequently, it was injected into 1 mL of Au NPs (~16 nm) and shaken overnight at room temperature.[20] Next, the solution of locked DNA nanomachines was salt-aged slowly by adding aliquots of a 2 M NaCl solution into the above solution to obtain the mixed solution and was kept for 10 h to achieve spherical DNA nanostructures with a high density of H1. Then, the obtained mixture was shaken overnight to obtain the H1-functionalized spherical nanostructures (named as locked DNA nanomachines). Finally, the locked DNA nanomachines were centrifuged at a rate of 12 000 rpm for 12 min at 4 °C, washed with binding buffer twice, and resuspended in 400 μL of binding buffer (consisting of 10 mM Tris, 120 mM NaCl, 5 mM KCl, and 20 mM $CaCl_2$) for further use.

2.3. Fabrication of the ECL Biosensor. The bare GCE (Φ = 4 mm) was handled based on the reported approach to achieve a smooth and clean surface.[21] Then, 12 μL of the hollow Pd-Rub-Ag@Au nanocube solution was coated onto the bare GCE to obtain the hollow Pd-Rub-Ag@Au nanocube-modified electrode (Pd-Rub-Ag@Au nanocubes/GCE). Subsequently, 10 μL of the solution of 2 μM quenching DNA hybridization product (C1-S1-S2) formed by annealing (as shown in the Supporting Information (SI) Section S1.1) was incubated on the resultant electrode overnight at 4 °C by a Pd−N bond to obtain C1-S1-S2/Pd-Rub-Ag@Au nanocubes/GCE. Eventually, 10 μL of 1 mM hexanethiol (HT) was incubated on the surface of the resultant electrode for 50 min at 25 °C to block nonspecific sites of the biosensor (HT/C1-S1-S2/Pd-Rub-Ag@Au nanocubes/GCE). Prior to each step of modification and measurement, the electrode was rinsed with deionized water.

2.4. Measurement Procedure. First, the sample solution consisting of 10 μL of the target OTA standard solution with different concentrations, 210 μL of 1 μM A1, 5 μL of 200 U/μL Exo III, 25 μL of 10× NEB buffer 2, and 280 μL of locked DNA nanomachines was incubated for 40 min at 37 °C to proceed the OTA-induced hairpin assembly enzyme-powered cyclic amplification, and then, the reaction process was terminated by incubation at 70 °C for 20 min, achieving the activation of multisite-anchored DNA nanomachines.

Subsequently, the reaction solution was obtained by mixing 250 μL of the resultant sample solution and 1 μM S3-Pd (the preparation method of S3-Pd is presented in Section S1.3 of the SI). Then, 10 μL of the reaction solution was dropped onto the surface of the proposed biosensor (HT/C1-S1-S2/Pd-Rub-Ag@Au nanocubes/GCE) to react at 25 °C for 30 min, executing the movement of multisite-anchored DNA nanomachines on the surface of the biosensor through the strand displacement reaction (SDR). Eventually, ECL response was recorded through the measurement of the biosensor in 3 mL of 0.1 M phosphate-buffered saline (PBS, pH 7.4) on an MPI-E ECL analytical system. The range of the working potential was set as −1.0 to 1.2 V at a scan rate of 0.25 V/s (magnitude 3, PMT high-voltage 800 V).

https://doi.org/10.1021/acs.analchem.1c00446
Anal. Chem. 2021, 93, 5301−5308

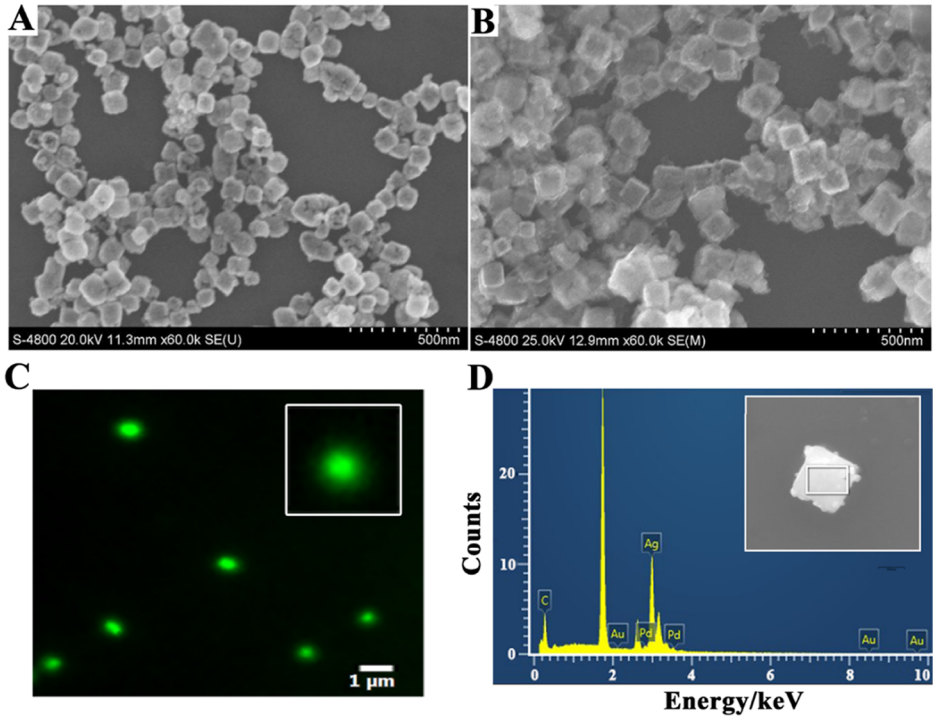

Figure 1. SEM image of (A) hollow Ag@Au nanocubes and (B) hollow Rub-Ag@Au nanocubes. (C) Pseudo-colored FL microscopic image of Rub-Ag@Au nanocubes. (D) EDS spectrum of the Pd-Rub-Ag@Au nanocubes; the inset of (D) shows the SEM image of the Pd-Rub-Ag@Au nanocubes.

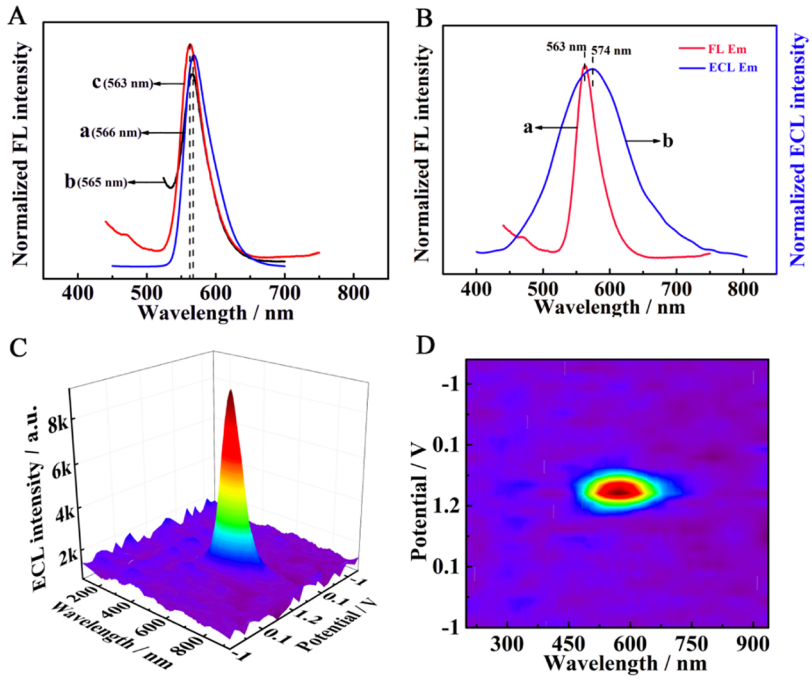

Figure 2. (A) Normalized FL spectra of (a) Rub in THF, (b) hollow Rub-Ag@Au nanocubes, and (c) hollow Pd-Rub-Ag@Au nanocubes in ultrapure water. (B) Normalized FL (curve *a*) and ECL (curve *b*) emission spectra of the hollow Pd-Rub-Ag@Au nanocubes. (C) 3D color map surface of the hollow Pd-Rub-Ag@Au nanocubes. (D) 3D heat map of ECL from the Pd-Rub-Ag@Au nanocubes.

3. RESULTS AND DISCUSSION

3.1. Structural Characterization of the Synthesized Nanomaterials. Scanning electron microscopy (SEM) was employed to observe the morphology of the synthesized nanomaterials directly. As displayed in Figure 1A, the Ag@Au nanocubes were well monodispersed and exhibited a hollow cubic frame structure with a uniform size distribution (edge length about 100 nm). After Rub^{+} was reduced with the hollow Ag@Au nanocubes as a template, the hollow Rub-Ag@Au nanocubes were achieved (Figure 1B), which had similar morphology and size as that of Ag@Au nanocubes, demonstrating that the frame structure of Ag@Au nanocubes was well preserved. And the Rub-Ag@Au nanocubes showed good fluorescence (FL) performance, as shown in Figure 1C. The

https://doi.org/10.1021/acs.analchem.1c00446
Anal. Chem. 2021, 93, 5301−5308

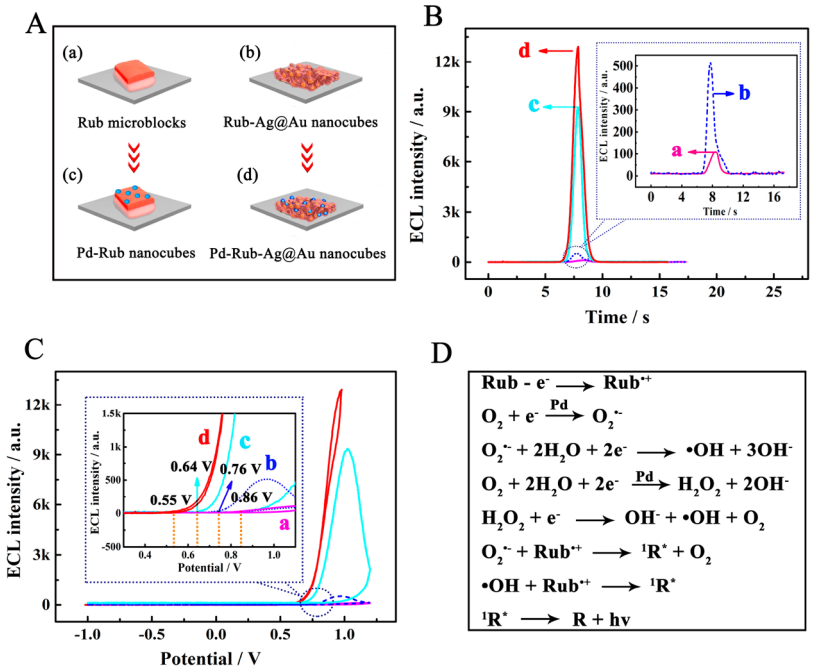

Figure 3. (A) Schematic diagrams of different nanomaterials modified electrodes, (a) Rub microblocks/GCE, (b) Rub-Ag@Au nanocubes/GCE, (c) Pd-Rub nanocubes/GCE, and (d) Pd-Rub-Ag@Au nanocubes/GCE. (B) ECL intensity−time and (C) ECL intensity−potential curves of (a) Rub microblocks/GCE, (b) Rub-Ag@Au nanocubes/GCE, (c) Pd-Rub nanocubes/GCE, and (d) Pd-Rub-Ag@Au nanocubes/GCE in PBS. (D) Possible ECL mechanism of the proposed ECL ternary system.

size and shape in the FL image were in good agreement with that in the SEM image (Figure 1B), confirming that Rub was obtained on the surface of Ag@Au nanocubes successfully. After Pd NPs were in situ reduced on a Rub-Ag@Au nanocubes surface, the morphology of Pd-Rub-Ag@Au nanocubes is exhibited in the inset of Figure 1D, which had similar morphology and size as that of Rub-Ag@Au nanocubes. The elemental composition of Pd-Rub-Ag@Au nanocubes was employed by energy-dispersive X-ray spectroscopy (EDS, Figure 1D), which contained Au, Ag, and Pd elements, further illustrating the generation of Pd-Rub-Ag@Au nanocubes.

3.2. Optical Characteristics of Hollow Pd-Rub-Ag@Au Nanocubes. To characterize the optical properties of different nanocubes, the FL and ECL spectra were investigated. As shown in Figure 2A, the FL emission peaks of the hollow Rub-Ag@Au nanocubes (curve *b*) and Pd-Rub-Ag@Au nanocubes (curve *c*) were at 565 and 563 nm, respectively, which were almost consistent with that of the monodispersed Rub (Rub in THF located at 566 nm, curve *a*). These results demonstrated that the Rub molecules existed in the form of monodispersed states in Pd-Rub-Ag@Au nanocubes, whose characteristic FL emission was unaffected by the hollow Ag@Au nanocubes and Pd NPs. As shown in Figure 2B, the ECL maximum wavelength of the hollow Pd-Rub-Ag@Au nanocubes at 574 nm (curve *b*) was extremely close to the FL maximum wavelength (curve *a*), illustrating that the excited states in the ECL process were probably in accordance with its photoluminescence process. In addition, the three-dimensional (3D) color map surface from the hollow Pd-Rub-Ag@Au nanocubes recorded their ECL evolution process in detail (Figure 2C). The typical heat map image of ECL from Pd-Rub-Ag@Au nanocubes displayed the maximum emission wavelength at 574 nm clearly and intuitively (Figure 2D).

3.3. ECL Relative Efficiency of Hollow Pd-Rub-Ag@Au Nanocubes. Figure 3A shows the schematic diagrams of different Rub nanomaterial-based electrodes: (a) Rub microblock-modified GCE (Rub microblocks/GCE), which was prepared according to the reported method,[6] (b) Rub-Ag@Au nanocube-modified GCE (Rub-Ag@Au nanocubes/GCE), (c) Pd NPs adsorbed on the surface of Rub microblocks/GCE (Pd-Rub nanocubes/GCE), and (d) the proposed Pd-Rub-Ag@Au nanocube-modified GCE (Pd-Rub-Ag@Au nanocubes/GCE). The corresponding ECL intensity−time and ECL intensity−potential curves are illustrated in Figure 3B,C to investigate the ECL characteristics of different Rub-based nanomaterials, with a potential scan cycle between −1.0 and 1.2 V. As displayed in Figure 3B, the ECL intensity of Rub microblocks/GCE (curve *a*) in PBS was observed at 109 au, while it reached 513 a.u. in the Rub-Ag@Au nanocubes/GCE. The faint ECL intensity could be attributed to the small number of free radicals produced by dissolved O_2. When Pd-Rub nanocubes/GCE was detected, it showed an obvious intensity at 9379 a.u. mainly due to the effect of a Pd NP accelerator on dissolved O_2 in comparison to the Rub microblocks/GCE. Surprisingly, a remarkably enhanced ECL signal at 12 918 a.u. was obtained at the proposed Pd-Rub-Ag@Au nanocubes/GCE, which was 25.2-fold higher than that of the Rub-Ag@Au nanocubes/GCE, and also higher than that of the Pd-Rub nanocubes/GCE. We could speculate that Pd NPs acted as the coreaction accelerator in the Rub/O_2 system to promote the production of reactive oxygen species (ROS), and the hollow Pd-Rub-Ag@Au nanocubes reduced the inner filter effect, achieving the strong ECL emission. Additionally, in comparison with the onset potential of Rub microblocks/GCE, Rub-Ag@Au nanocubes/GCE and Pd-Rub nanocubes/GCE at 0.86, 0.76, and 0.64 V, respectively, the more negative oxidation potential of Pd-Rub-Ag@Au nanocubes/GCE at 0.55 V was just needed, demonstrating that the ECL reaction was much easier on the proposed Rub/O_2/Pd NPs ternary system. The possible ECL mechanism of Pd-Rub-Ag@Au nanocubes is displayed in Figure 3D.

https://doi.org/10.1021/acs.analchem.1c00446
Anal. Chem. 2021, 93, 5301−5308

The ECL relative quantum efficiency (Φ) was calculated by the ratio of the ECL intensity to the amount of electrochemically oxidized hollow Pd-Rub-Ag@Au nanocubes.[22] First, the ECL responses of Rub microblocks/GCE, Rub-Ag@Au nanocubes/GCE, and Pd-Rub-Ag@Au nanocubes/GCE in 0.1 M PBS were obtained, respectively. Then, the charges of the oxidation (Q) from Rub microblocks, Rub-Ag@Au nanocubes, and Pd-Rub-Ag@Au nanocubes were acquired by the integral during the scanning process. According to eq 1, the number of electrochemically oxidized Rub microblocks, Rub-Ag@Au nanocubes, and Pd-Rub-Ag@Au nanocubes could be calculated roughly. Among them, z is the number of transferred electrons for per molecule and F is Faraday's constant. Subsequently, ECL Φ was calculated according to eq 2.

$$n = Q/zF \quad (1)$$

$$\Phi = k\, I_{ECL}/n_{rub} \quad (2)$$

The results of ECL relative Φ for different nanomaterials are presented in Table 1. The ECL relative Φ of Rub microblocks was defined as 1, where the ECL quantum efficiencies of Rub-Ag@Au nanocubes and Pd-Rub-Ag@Au nanocubes were about 1.95 and 8.23 times higher than that of Rub microblocks, respectively. Therefore, the ECL efficiency of the hollow Pd-Rub-Ag@Au nanocubes was proved greatly compared with that of Rub microblocks and Rub-Ag@Au nanocubes.

Table 1. ECL Relative Φ of Hollow Pd-Rub-Ag@Au Nanocubes

state	I_{ECL}	Q	Φ′
Rub microblocks/GCE	109	0.608	1
Rub-Ag@Au nanocubes/GCE	513	0.414	1.95
Pd-Rub-Ag@Au nanocubes/GCE	12 918	1.524	8.23

3.4. Reaction Rate of Multisite-Anchored DNA Nanomachines. To demonstrate the reaction rate of the proposed multisite-anchored DNA nanomachine, the ECL responses with different DNA nanomachines were obtained by the single-leg DNA walker (Figure 4A) and multisite-anchored DNA nanomachine (proposed DNA nanomachine, Figure 4D), respectively. Namely, the nanomachines of the single-leg DNA walker and the proposed nanomachine were incubated with the prepared biosensor to conduct S3-driven SDR under the same experimental conditions. Then, the two types of resultant electrodes were measured in 3 mL of PBS (0.1 M, pH 7.4). The ECL response of the single-leg DNA walker increased with the reaction time, and the ECL intensity reached a plateau after 105 min (Figure 4B). Amazingly, the comparative ECL intensity was achieved within a shorter time of 30 min by the multisite-anchored DNA nanomachine (Figure 4E). Moreover, on comparing the slopes of the time-dependent ECL curves, the proposed multisite-anchored DNA nanomachine (k = 455.5, Figure 4F) exhibited a larger value of the slope compared with that of the single-leg DNA walker (k = 133.6, Figure 4C), illustrating that the proposed multisite-anchored DNA nanomachines possessed the faster reaction rate.

3.5. Performance Research of the Biosensor. ECL responses of the proposed biosensor for detecting OTA with different concentrations were measured under the optimal experimental parameters. As displayed in Figure 5A, the ECL signal enhanced gradually along with the increasing concentration of OTA within the range from 0.01 to 100 pg/mL. As a result, there was a linear relationship between the ECL intensity (I_{ECL}) and the logarithm of the OTA concentration (lg c) in Figure 5B. The calibration plot was expressed as I_{ECL} = 6708.17 + 2456.95 lg c with a correlation coefficient (R) of 0.997. In addition, the detection limit was 4.7 fg/mL (S/N = 3) (see the Section S1.6 of SI). Furthermore, in comparison with the results reported in previous work (Table 2), the proposed biosensor exhibited an outstanding analytical performance for OTA detection.

The selectivity and stability were two significant parameters to evaluate the specificity and practicability of the proposed ECL

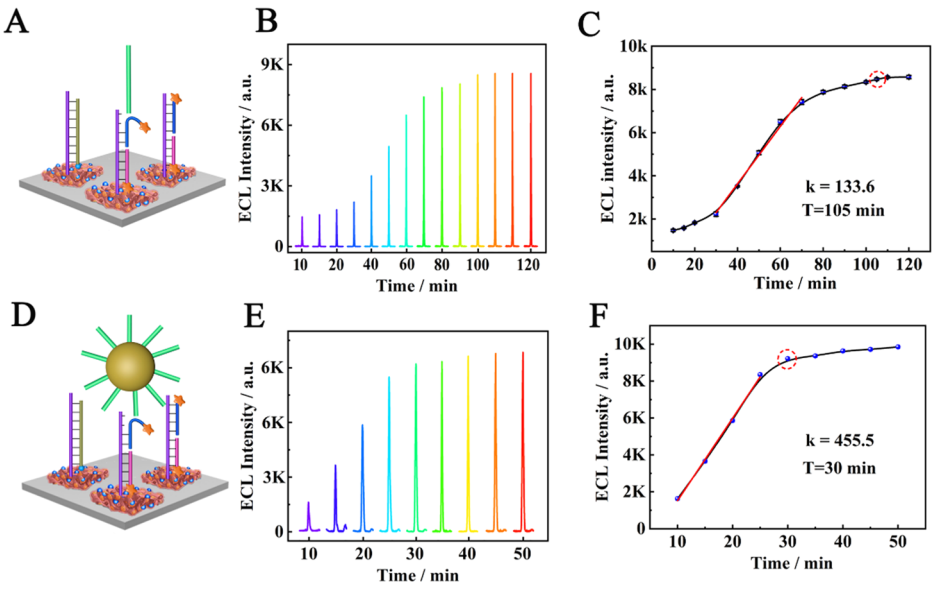

Figure 4. ECL responses of the biosensor using different DNA nanomachines with 10 nM of target OTA: (A) single-leg DNA walker and (D) multisite-anchored DNA nanomachine. ECL response curves of the (B) single-leg DNA walker and the (E) multisite-anchored DNA nanomachine-based biosensor as a function of time. The ECL changing trend of the (C) single-leg DNA walker and the (F) multisite-anchored DNA nanomachine on the surface of the biosensor.

https://doi.org/10.1021/acs.analchem.1c00446
Anal. Chem. 2021, 93, 5301−5308

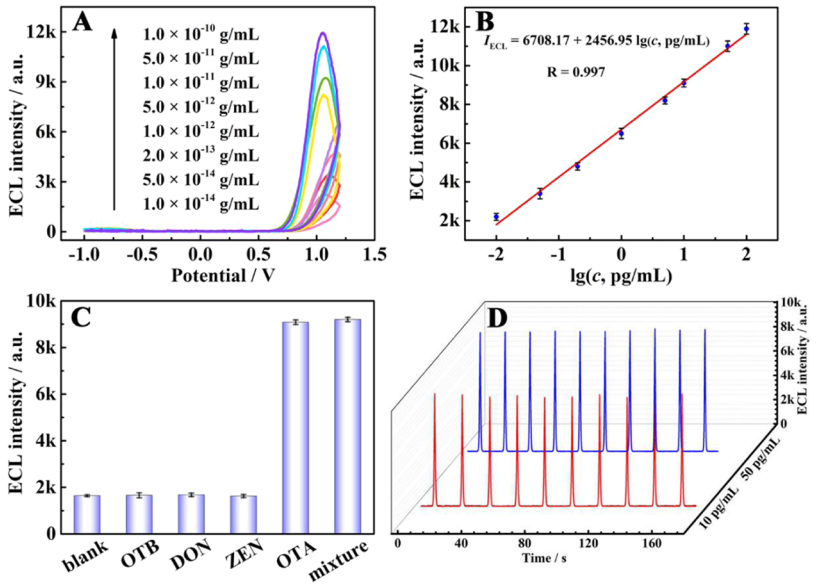

Figure 5. (A) ECL intensity−potential profiles of the proposed ECL biosensor with various concentrations of the target OTA (0.01−100 pg/mL). (B) Corresponding calibrating plot of the proposed biosensor for OTA detection (error bars, SD, $n = 3$). (C) Selectivity of the ECL biosensor with relevant interfering molecules. (D) Stability of the ECL biosensor in the presence of OTA (10 and 50 pg/mL).

Table 2. Comparison of Different Methods for OTA Detection

detection method	liner range	limit of detection	references
ECL	0.02−2 ng/mL	4.8 pg/mL	23
ECL	0.0002−1 ng/mL	75 fg/mL	24
FL	0.01−100 ng/mL	3 pg/mL	25
electrochemistry	0.01−5 ng/mL	5 pg/mL	26
ECL	1.0×10^{-14}−1.0×10^{-10} g/mL	4.7 fg/mL	this work

biosensor. First, some relevant interfering molecules including ochratoxin B (OTB), vomitoxin (DON), and zearalenone (ZEN) with identical concentration (100 pg/mL) were employed as interfering substances to execute experiments for comparisons. As depicted in Figure 5C, despite the higher concentration of interfering molecules, there were semblable ECL signals with that of the blank sample (the target OTA methanol solution was replaced by the same volume methanol). However, noticeable enhancement of ECL intensity was observed with the mixture containing the relevant interfering molecules and OTA. It was implied that the proposed ECL strategy had excellent selectivity for OTA detection. Additionally, the stability of the biosensor was investigated by monitoring the ECL responses under continuous scans in 0.1 M PBS (pH 7.4). As demonstrated in Figure 5D, the ECL intensity of the biosensor remained almost unchanged within 10 cycles, which suggested that the biosensor possessed excellent stability.

3.6. Analysis of OTA in White Wine. The recovery of OTA with known concentrations in white wine was applied to assess the feasibility and accuracy of the as-designed approach. First, 5 mL of white wine (bought from a local supermarket chain) was pretreated by adding 0.05 g of poly(vinylpyrrolidone) K30 to remove the precipitate via filtration. Next, the collected filtrate was adjusted to pH 7.0−7.2, and then the resultant solution was mixed with A1, Exo III, 10× NEB buffer 2, locked DNA nanomachines, and the OTA with different concentrations (0.01, 0.5, 10, and 50 pg/mL) to prepare the reaction solution for detection. The recovery and relative standard deviations (RSD) of OTA are displayed in Table 3, where the range of recovery and RSD are 94.6−112.0 and 3.4−4.3%, respectively.

Table 3. Recovery of OTA in White Wine

sample number	added (pg/mL)	detected (pg/mL)	recovery (%)	RSD (%)
1	0.01	0.011	112.0	3.9
2	0.20	0.189	94.6	3.5
3	5.00	5.236	104.0	3.4
4	50.0	52.74	105.0	4.3

Based on these results, it clearly illustrated that the proposed biosensor could serve as a potential tool for OTA detection in real samples.

4. CONCLUSIONS

In conclusion, an efficient and sensitive biosensor was constructed for OTA detection by combining the advantages of the advanced hollow Pd-Rub-Ag@Au nanocubes with multisite-anchored DNA nanomachines in this work. Above all, it was worth noting that the hollow Pd-Rub-Ag@Au nanocubes as the ECL luminophores were first prepared by an in situ redox deposition method, which could reduce the inner filter effect and improve the ECL efficiency in aqueous media. More significantly, the multisite-anchored DNA nanomachine processed a fast reaction rate as the high local effective concentration of signal probe-recognizing sequences, which could be assigned to their multiple sites to operate simultaneously on the sensing platform and accelerate the movement efficiency and velocity. Our success in designing the multisite-anchored DNA nanomachine pointed a new direction for the development of novel DNA nanodevices and biosensors.

https://doi.org/10.1021/acs.analchem.1c00446
Anal. Chem. 2021, 93, 5301−5308

■ ASSOCIATED CONTENT

Supporting Information

The Supporting Information is available free of charge at https://pubs.acs.org/doi/10.1021/acs.analchem.1c00446.

Chemicals and materials, apparatus, preparation of Pd NPs and S3-Pd, ECL and CV characterization of the ECL biosensor, optimization of the reaction conditions, and the calculation procedure of the LOD and ECL relative efficiency (PDF)

■ AUTHOR INFORMATION

Corresponding Author

Ying Zhuo − *Key Laboratory of Luminescence Analysis and Molecular Sensing (Southwest University), Ministry of Education, College of Chemistry and Chemical Engineering, Southwest University, Chongqing 400715, P. R. China;* orcid.org/0000-0002-4491-1186; Phone: +86 23 68253172; Email: yingzhuo@swu.edu.cn

Authors

Xia Zhong − *Key Laboratory of Luminescence Analysis and Molecular Sensing (Southwest University), Ministry of Education, College of Chemistry and Chemical Engineering, Southwest University, Chongqing 400715, P. R. China*

Shan-Shan Yang − *Key Laboratory of Luminescence Analysis and Molecular Sensing (Southwest University), Ministry of Education, College of Chemistry and Chemical Engineering, Southwest University, Chongqing 400715, P. R. China*

Ni Liao − *Key Laboratory of Luminescence Analysis and Molecular Sensing (Southwest University), Ministry of Education, College of Chemistry and Chemical Engineering, Southwest University, Chongqing 400715, P. R. China; College of Biological and Chemical Engineering, Panzhihua University, Panzhihua 617000, P. R. China*

Ruo Yuan − *Key Laboratory of Luminescence Analysis and Molecular Sensing (Southwest University), Ministry of Education, College of Chemistry and Chemical Engineering, Southwest University, Chongqing 400715, P. R. China;* orcid.org/0000-0003-3664-6236

Complete contact information is available at: https://pubs.acs.org/10.1021/acs.analchem.1c00446

Author Contributions

§X.Z. and S.-S.Y. contributed equally to this work.

Notes

The authors declare no competing financial interest.

■ ACKNOWLEDGMENTS

This work was financially supported by the NNSF of China (21904108, 22022408), the Chongqing Talents Personnel Support Program (CQYC201905067), and the Fundamental Research Funds for the Central Universities (XDJK2019TJ002), China.

■ REFERENCES

(1) Jiang, M. H.; Li, S. K.; Zhong, X.; Liang, W. B.; Chai, Y. Q.; Zhuo, Y.; Yuan, R. *Anal. Chem.* **2019**, *91*, 3710−3716.

(2) Qi, H.; Chen, Y. H.; Cheng, C. H.; Bard, A. J. *J. Am. Chem. Soc.* **2013**, *135*, 9041−9049.

(3) Liu, W.; Chen, A. Y.; Li, S. K.; Peng, K. F.; Chai, Y. Q.; Yuan, R. *Anal. Chem.* **2019**, *91*, 1516−1523.

(4) Zhao, M. L.; Zeng, W. J.; Chai, Y.Q.; Yuan, R.; Zhuo, Y. *Anal. Chem.* **2020**, *92*, 11044−11052.

(5) Liu, J. L.; Tang, Z. L.; Zhuo, Y.; Chai, Y. Q.; Yuan, R. *Anal. Chem.* **2017**, *89*, 9108−9115.

(6) Yang, S. S.; Jiang, M. H.; Chai, Y. Q.; Yuan, R.; Zhuo, Y. *ACS Appl. Mater. Interfaces* **2018**, *10*, 38648−38655.

(7) Bilger, J. B.; Kerzig, C.; Larsen, C. B.; Wenger, O. S. *J. Am. Chem. Soc.* **2021**, *143*, 1651−1663.

(8) Liu, J. L.; Zhang, J. Q.; Tang, Z. L.; Chai, Y. Q.; Zhuo, Y.; Yuan, R. *Chem. Sci.* **2019**, *10*, 4497−4501.

(9) Xuan, F.; Hsing, I. M. *J. Am. Chem. Soc.* **2014**, *136*, 9810−9813.

(10) Bai, M.; Chen, F.; Cao, X. W.; Zhao, Y.; Xue, J.; Yu, X.; Fan, C. H.; Zhao, Y. X. *Angew. Chem.* **2020**, *132*, 13369−13374.

(11) Li, Y. K.; Deng, J. Q.; Han, Z. W.; Liu, C.; Tian, F.; Xu, R.; Han, D.; Zhang, S. H.; Sun, J. S. *J. Am. Chem. Soc.* **2021**, *143*, 1290−1295.

(12) Chen, F.; Xue, J.; Zhang, J.; Bai, M.; Yu, X.; Fan, C. H.; Zhao, Y. X. *J. Am. Chem. Soc.* **2020**, *142*, 2889−2896.

(13) Yang, X. L.; Tang, Y. N.; Mason, S. D.; Chen, J. B.; Li, F. *ACS Nano* **2016**, *10*, 2324−2330.

(14) Zhang, P.; Jiang, J.; Yuan, R.; Zhuo, Y.; Chai, Y. Q. *J. Am. Chem. Soc.* **2018**, *140*, 9361−9364.

(15) Huang, X. B.; Wu, S. H.; Hu, H. C.; Sun, J. J. *ACS Sens.* **2020**, *5*, 2636−2643.

(16) Wang, C.; Kuang, Y.; Luo, L.; Sun, X. M. *J. Mater. Chem. C* **2013**, *1*, 4146−4152.

(17) Li, J. R.; Zhang, G. N.; Wang, J.; Maksymov, I. S.; Greentree, A. D.; Hu, J. M.; Shen, A. G.; Wang, Y. L.; Trau, M. *ACS Appl. Mater. Interfaces* **2018**, *10*, 32526−32535.

(18) Yang, L.; Li, Y. Y.; Zhang, Y.; Fan, D. W.; Pang, X. H.; Wei, Q.; Du, B. *ACS Appl. Mater. Interfaces* **2017**, *9*, 35260−35267.

(19) Xu, J. M.; Zhang, Y.; Li, L.; Kong, Q. K.; Zhang, L. N.; Ge, S. G.; Yu, J. H. *ACS Appl. Mater. Interfaces* **2018**, *10*, 3431−3440.

(20) Enustun, B. V.; Turkevich, J. *J. Am. Chem. Soc.* **1963**, *85*, 3317−3328.

(21) Pan, M. C.; Lei, Y. M.; Chai, Y. Q.; Yuan, R.; Zhuo, Y. *Anal. Chem.* **2020**, *92*, 13581−13587.

(22) Qiao, Y. L.; Li, Y.; Fu, W.; Guo, Z. H.; Zheng, X. W. *Anal. Chem.* **2018**, *90*, 9629−9636.

(23) Wei, M.; Wang, C. L.; Xu, E. S.; Chen, J.; Xu, X. L.; Wei, W.; Liu, S. Q. *Food Chem.* **2019**, *282*, 141−146.

(24) Chen, Y.; Yang, M. L.; Xiang, Y.; Yuan, R.; Chai, Y. Q. *Nanoscale* **2014**, *6*, 1099−1104.

(25) Wang, C. Q.; Qian, J.; Wang, K.; Hua, M. J.; Liu, Q.; Hao, N.; You, T.; Huang, X. Y. *ACS Appl. Mater. Interfaces* **2015**, *7*, 26865−26873.

(26) Shi, L.; Rong, X. J.; Wang, Y.; Ding, S. M.; Tang, W. Y. *Biosens. Bioelectron.* **2018**, *102*, 41−48.